

P-orbital magnetic topological states on square lattice

Jing-Yang You,^{1,2} Bo Gu,^{1,3} and Gang Su^{1,3,4}

¹*Kavli Institute for Theoretical Sciences, and CAS Center for Excellence in Topological Quantum Computation, University of Chinese Academy of Sciences, Beijing 100190, China*

²*Department of Physics, Faculty of Science, National University of Singapore, 117551, Singapore*

³*Physical Science Laboratory, Huairou National Comprehensive Science Center, Beijing 101400, China*

⁴*School of Physical Sciences, University of Chinese Academy of Sciences, Beijing 100049, China*

Honeycomb or triangular lattices were extensively studied and thought to be proper platforms for realizing quantum anomalous Hall effect (QAHE), where magnetism is usually caused by *d* orbitals of transition metals. Here we propose that square lattice can host three magnetic topological states, including the fully spin polarized nodal loop semimetal, QAHE and topologically trivial ferromagnetic semiconductor, in terms of the symmetry and *k* · *p* model analyses that are materials-independent. A phase diagram is presented. We further show that the above three magnetic topological states can be indeed implemented in two-dimensional (2D) materials ScLiCl₅, LiScZ₅ (Z=Cl, Br), and ScLiBr₅, respectively. The ferromagnetism in these 2D materials is microscopically revealed from *p* electrons of halogen atoms. This present study opens a door to explore the exotic topological states as well as quantum magnetism from *p*-orbital electrons by means of the materials-independent approach.

Introduction—In two-dimensional (2D) systems, the coexistence of magnetism and nontrivial topological states can induce many novel physical phenomena. A typical example is the quantum anomalous Hall effect (QAHE), where the combination of ferromagnetism and topological insulator can generate dissipationless edge states at boundaries^{1–6}. The quantized Hall conductivity is carried by the edge states, which is robust against disorders and impurities. Owing to the dissipationless chiral edge states, QAHE would have potential applications in ultralow-power consumption spintronic devices⁷. Thus, the search for materials with QAHE has attracted extensive interests^{3,8–12}. Since the seminal work of Haldane¹, the honeycomb lattice is thought to be a proper platform to realize the QAHE, e.g., several ferromagnetic transition metal trihalides with honeycomb lattice were proposed to be candidates for the implementation of QAHE^{13–19}. Besides, the experimental observation of QAHE was realized in magnetic atom doped systems^{10,20–22}, and recently in the few layers of magnetic semiconductor MnBi₂Te₄^{23–26} with triangular lattice. In these materials, *d* orbitals of the transition metal play important roles in realizing QAHE. Two interesting questions then arise: whether can the QAHE be realized in other lattices, such as square lattice? Can the QAHE be obtained in materials with *p* orbitals? The study on these questions cannot only give a further understanding of topological states and quantum magnetism, but also offer new family of materials to search for possible room temperature QAHE.

In this work, we address these appealing issues by revealing a square lattice with the space group P/4n (No.85) that can accommodate three different *p*-orbital magnetic topological states, i.e. the fully spin-polarized nodal loop semimetal, QAHE and ferromagnetic semiconductor. These three quantum states can be obtained by the symmetry and *k* · *p* model analysis, which can be implemented in 2D materials ScLiCl₅, LiScZ₅ (Z=Cl,

Br), and ScLiBr₅. It is shown that the ferromagnetism in these 2D materials is attributed to *p* orbitals. Our findings provide a new mechanism of magnetic topological states from *p*-orbital electrons on square lattices, and also present a novel family of 2D magnetic topological materials with high Chern number.

Three magnetic topological states on square lattice—

Let us consider a square lattice with the space group of P/4n (No.85) for *p* orbitals. There are three generators: four-fold rotation symmetry $C_4: (x, y, z) \rightarrow (y, -x, z)$, roto-inversion symmetry $\tilde{I}: (x, y, z) \rightarrow (\frac{1}{2} - x, \frac{1}{2} - y, -z)$ and glide mirror symmetry $\tilde{M}_z: (x, y, z) \rightarrow (\frac{1}{2} + x, \frac{1}{2} + y, -z)$. The symmetry protected double degeneracy appears at high-symmetry points in the absence of SOC as shown in Fig. 1(a). Without SOC, the spin and orbital parts of the electronic wave functions are decoupled, and hence all crystalline symmetries are preserved for each spin channel separately like spinless particles. For the whole BZ, the glide mirror \tilde{M}_z is preserved. The high symmetry points Γ, X, Y and M are invariant under the combined operation $T\tilde{M}_z$. We note that $(T\tilde{M}_z)^2 = T_{110}$, where $T^2 = 1$ for the spinless case, and $T_{110} = e^{-ik_x - ik_y}$ represents the translation by one unit cell along the [110] direction. At X point, we have $k_x = \pi$ and $k_y = 0$, while at Y point, we have $k_x = 0$ and $k_y = \pi$. Consequently, $(T\tilde{M}_z)^2 = -1$ for X and Y points. This antiunitary operator thus generates a Kramers-like double degeneracy at X and Y points. One may note that M point is invariant under both C_4 and \tilde{I} . The commutation relation between C_4 and \tilde{I} is given by $C_4\tilde{I} = T_{0\bar{1}0}\tilde{I}C_4$, where $T_{0\bar{1}0} = e^{ik_y}$. At M point, we have $k_x = \pi$ and $k_y = \pi$; hence, $T_{0\bar{1}0} = -1$. As a result, for any energy eigenstate $|u\rangle$ with C_4 eigenvalue E_z , it must have a degenerate partner $\tilde{I}|u\rangle$ with C_4 eigenvalue $-E_z$. This proves that the double degeneracy at M is guaranteed by the symmetry. At Γ point p_x and p_y orbitals should be degenerate, while p_z orbitals are not.

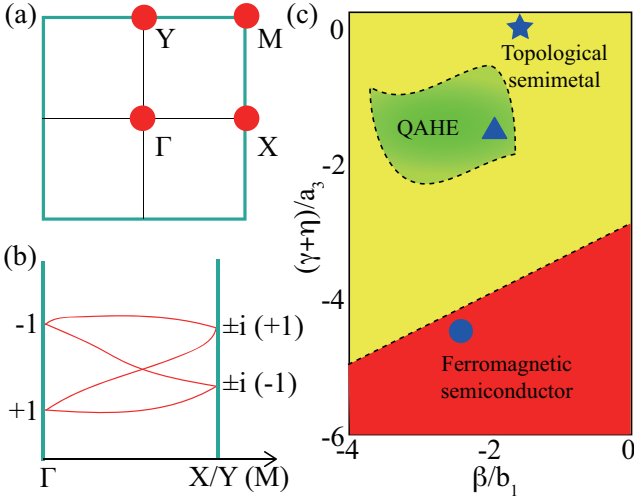


FIG. 1. The square lattice with three magnetic topological states. (a) Schematic illustration of the double degeneracy at high symmetry points (red dots). (b) Schematic depiction of hourglass dispersion along $\Gamma - X/Y$ and $\Gamma - M$ high symmetry lines. The labels indicate the eigenvalues of \widetilde{M}_z . (c) Schematic phase diagram with respect to the parameters $(\gamma + \eta)/a_3$ and β/b_1 in Eq. (1), where yellow, red and green regions represent topological semimetal, topologically trivial ferromagnetic semiconductor and QAHE states, respectively.

Now we turn to discuss the possible band crossing at high symmetry lines. Consider $\Gamma - X$ and $\Gamma - M$ lines, which are invariant under \widetilde{M}_z . The Bloch states along $\Gamma - X$ can be chosen as the eigenstates of \widetilde{M}_z with eigenvalues $E_z = \pm e^{-ik_x/2}$. The glide eigenvalues are $\pm i$ at X and ± 1 at Γ . Because Γ and X are both time-reversal-invariant momenta, a Kramers pair has eigenvalues $(+i, -i)$ at X , and yet it has $(+1, +1)$ or $(-1, -1)$ at Γ . This suggests that the pairs must switch partners when going from X to Γ , and the switching leads to the hourglass-type dispersion, as schematically shown in Fig. 1(b). A similar analysis applied for path $\Gamma - Y$ shows that the band crossing is also hourglass-type along $\Gamma - Y$. The Bloch states along $\Gamma - M$ have the eigenstates of \widetilde{M}_z with eigenvalues $E_z = \pm e^{-ik_x/2 - ik_y/2}$. The glide eigenvalues are ± 1 at both M and Γ . Because Γ and M are both time-reversal-invariant momenta, a Kramers pair has eigenvalues $(+1, +1)$ and $(-1, -1)$ at M and Γ , leading to the hourglass-type crossing along $\Gamma - M$ [Fig. 1(b)]. The crossing point may trace out a nodal loop centered at Γ .

To characterize the above discussed band crossing, we construct an effective $k \cdot p$ model for the low-energy band structure on square lattice. We first consider the case without SOC. The four states at Γ point correspond to two 2D irreducible representations E_u and E_g . The model should respect the following symmetries: the four-fold rotation C_{4z} , and the mirror symmetry M_z . Expanding up to the k quadratic order, we find that the effective

Hamiltonian takes the form of

$$H_0 = \begin{pmatrix} a(k) & -ic(k) & 0 & 0 \\ ic(k) & a(k) & 0 & 0 \\ 0 & 0 & b(k) & -id(k) \\ 0 & 0 & id(k) & b(k) \end{pmatrix},$$

where $a(k) = a_1 + a_2 k^2$, $b(k) = b_1 + b_2 k^2$, $c(k) = a_3 + a_4 k^2$, $d(k) = b_3 + b_4 k^2$, $k^2 = k_x^2 + k_y^2$, and the parameters a_i and b_i ($i=1,2,3,4$) are real. Considering a fully spin polarized ferromagnet, the inclusion of SOC gives additional contribution to the above Hamiltonian, which can be treated as a perturbation due to the relatively weak SOC strength. We find that the SOC term up to the leading order takes the following form:

$$H_{\text{SOC}} = \begin{pmatrix} \alpha & \gamma - \gamma i & 0 & 0 \\ \gamma + \gamma i & \alpha & 0 & 0 \\ 0 & 0 & \beta & \eta - \eta i \\ 0 & 0 & \eta + \eta i & \beta \end{pmatrix},$$

with real parameters α , β , γ and η . Thus, the total Hamiltonian reads

$$H = H_0 + H_{\text{SOC}}. \quad (1)$$

Due to the two-fold degeneracy at Γ point in the presence of SOC, we can obtain $a_1 = b_1$ and $a_3 = b_3$. If we fix $\beta = -\alpha$, a schematic phase diagram of the ratio of $(\gamma + \eta)/a_3$ as a function of β/b_1 can be drawn as shown in Fig. 1(c). Obviously, the SOC term will break the degeneracies at Γ point. It may also affect the degeneracy of the nodal loop, i.e. the nodal loop can be preserved with its shape and size changed slightly or the nodal loop vanishes with a band gap opened, and the system becomes QAH insulators or topologically trivial ferromagnetic semiconductors. From Fig. 1(c), one may note that topologically trivial ferromagnetic semiconductor appears in the region where the SOC parameters β and $\gamma + \eta$ has relative large absolute values, and topologically nontrivial states including nodal loop semimetal and topological insulator (QAHE) depend on the relationship and competition between β and $\gamma + \eta$. For the QAHE, the band inversion occurs.

Magnetic topological materials with square lattice—We now present several 2D material examples to implement the above different topological states, i.e. topological semimetal, topologically trivial ferromagnetic semiconductor and QAHE states as indicated in Fig. 1(c). These 2D materials with the formula unit XYZ_5 possess square lattice with the space group of $P/4n$, where X atoms occupy the Wyckoff position $2b(0; 0; 0.5)$, Y atoms occupy the Wyckoff position $2c(0.5; 0; 0.56383)$, and Z atoms occupy the Wyckoff positions $8g(0.20444, 0.11338, 0.59774)$ and $2c(0.5, 0, 0.40678)$ as shown in Fig. 2(a). It is interesting to mention that several bulk materials with similar structures had been synthesized and extensively studied in the last decades²⁷⁻³³.

Fully Spin-polarized Nodal Loop Semimetal in ScLiCl_5 —The structure of ScLiCl_5 monolayer with a

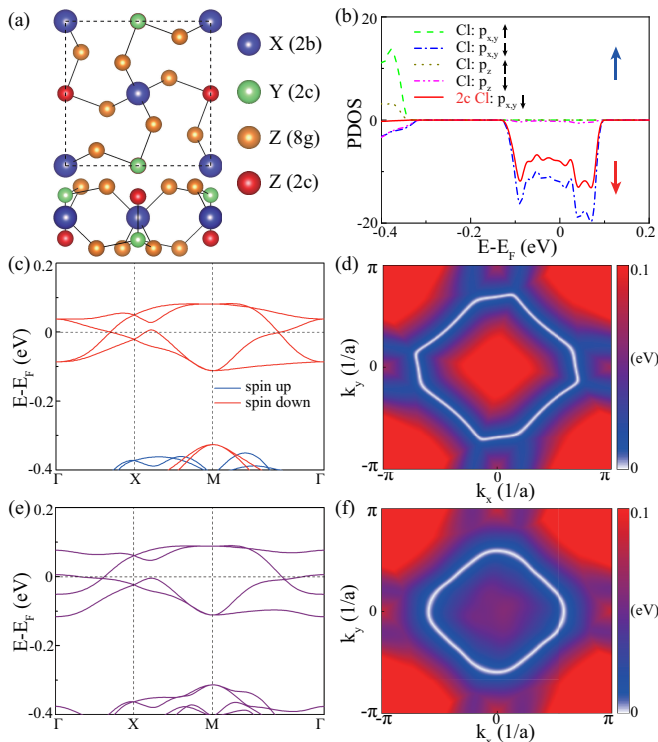


FIG. 2. Fully spin-polarized nodal loop semimetal ScLiCl_5 monolayer. (a) Top and side views of 2D materials XYZ_5 , where X atoms occupy the Wyckoff position $2b(0; 0; 0.5)$ colored in blue, Y atoms occupy the Wyckoff position $2c(0.5; 0; 0.56383)$ colored in green, and Z atoms occupy the Wyckoff positions $8g(0.20444, 0.11338, 0.59774)$ (orange) and $2c(0.5, 0, 0.40678)$ (red). (b) Partial density of states, (c) band structure and (d) the Weyl loop obtained from DFT calculations in the absence of SOC for ScLiCl_5 monolayer. (e) Electronic band structure and (f) the Weyl loop obtained from DFT calculations of ScLiCl_5 with SOC.

square lattice is depicted in Fig. 2(a). Each primitive cell contains two formula units of XYZ_5 . To confirm the stability of ScLiCl_5 monolayer, its phonon spectra have been calculated. There is no imaginary frequency mode in the whole Brillouin zone, indicating that this monolayer is dynamically stable. The structural stability of ScLiCl_5 monolayer is also examined in terms of the formation energy. The obtained negative values of formation energy (the energy difference between XYZ_5 and X, Y crystals, Z_2 molecule) for XYZ_5 monolayers are indicative of an exothermic reaction. Moreover, the thermal stability of ScLiCl_5 monolayer is tested by using the molecular dynamics simulation by considering a $3 \times 3 \times 1$ supercell of ScLiCl_5 with 126 atoms. After being heated at 300 K for 6 ps with a time step of 3 fs, no structural changes occur, indicating that this monolayer is also thermodynamically stable. More details can be found in Supplemental Materials (SM).

The optimized lattice constant of ScLiCl_5 monolayer is $a_0 = 7.9372 \text{ \AA}$. By a spin-polarized calculation, we note that the total spin magnetic moment carried by ScLiCl_5

is about $1.53 \mu_B$ per unit cell, which is mainly attributed to the two Cl atoms on Wyckoff position $2c$ (colored by red in Fig. 2(a)), whose spin and orbital moments are of about 0.50 and $0.16 \mu_B$ per atom, respectively. The ferromagnetism is mainly originated from the p orbitals of Cl atoms, whereas the spin magnetic moment on Sc atom is calculated to be zero. It is well interpreted that, for ScLiCl_5 , because Li and Sc have one and three valence electrons, respectively, Cl atoms possess unpaired electrons and thus should carry a nonzero spin magnetic moment. To determine the magnetic ground state, we compared the total energies between FM, antiferromagnetic (AFM) and non-magnetic (NM) states. The FM state is found to be more stable than AFM and NM states.

The partial density of states (PDOS) and electronic band structure in the absence of SOC are shown in Figs. 2(b) and (c), respectively. One observes that the material is a half-metal, with only one spin channel (spin down) being metallic and another spin channel (spin up) being insulating. From the projected density of states (PDOS) as displayed in Fig. 2(b), one may see that the states around the Fermi energy are fully polarized in the spin down channel, while the spin up channel has a large gap. In addition, the low-energy states are dominated by the $p_{x,y}$ orbitals of the Cl atoms on Wyckoff position $2c$. From Fig. 2(c), we find two features of the band structure. One is the double degeneracy at high symmetry points Γ , X and M , and another is the linear band-crossing points appearing on the paths Γ - X , and Γ - M . These crossing points are not isolated, and form a nodal loop around Γ point as shown in Fig. 2(d).

In the presence of SOC, the magnetic anisotropy should be considered. In order to determine the easy axis of magnetization, we shall pin down the magnetization direction for FM configurations. By comparing the energies of different magnetization directions, we find that the out-of-plane direction is energetically preferred over the in-plane directions and along that they are isotropic. We have also estimated the Curie temperature T_C for the FM state by using the Monte Carlo simulation based on an effective Hamiltonian

$$H_{spin} = \sum_{\langle i,j \rangle} J_1 S_i^z S_j^z + \sum_{\langle\langle i,j \rangle\rangle} J_2 S_i^z S_j^z, \quad (2)$$

where the spin vectors are normalized, the superscripts i and j label the $2c$ Cl sites, $\langle i,j \rangle$ and $\langle\langle i,j \rangle\rangle$ indicate nearest-neighboring and next nearest-neighboring sites, respectively, J_1 and J_2 are the corresponding FM exchange integrals. The values of J_1 and J_2 extracted from DFT calculations are -4.572 and -0.161 meV , respectively. The calculated Curie temperature for monolayer ScLiCl_5 is about 123 K.

The electronic band structure with SOC for ScLiCl_5 monolayer is shown in Fig. 2(e). It is noted that, the SOC only breaks the degeneracy at Γ point, but keeps the degeneracies at X (Y) and M points, which are protected by symmetry. The nodal loop is also preserved with SOC in monolayer ScLiCl_5 as shown in Fig. 2(f).

Thus, ScLiCl_5 monolayer exhibits a fully spin-polarized nodal loop semimetal (we could call it as nodal loop half-semimetal). By fitting the two bands near Fermi level, we can obtain the parameters for ScLiCl_5 : $\beta/a_1 = -1.4$ and $(\gamma + \eta)/a_3 = 0$. Thus, ScLiCl_5 locates in the region of topological semimetal as marked by a star in Fig. 1(c).

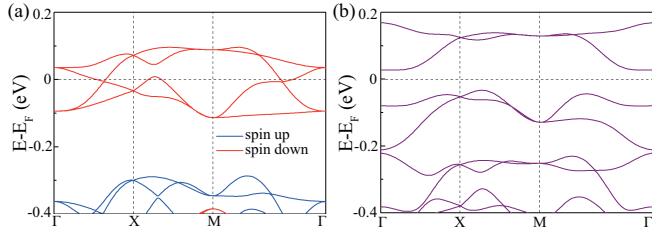


FIG. 3. Ferromagnetic semiconductor ScLiBr_5 monolayer. The electronic band structure (a) without SOC and (b) with SOC.

Ferromagnetic semiconductor in ScLiBr_5 —The monolayer ScLiBr_5 shares the same structure as ScLiCl_5 , except a larger lattice constant $a = 8.4175 \text{ \AA}$. The stability of monolayer ScLiBr_5 is also checked by its phonon spectra, molecular dynamics and formation energy, indicating it is feasible in experiment (see SM). The spin-polarized calculation shows that the total spin magnetic moment of ScLiBr_5 is about $1.43 \mu_B$ per unit cell, and the two Br atoms on Wyckoff position $2c$ possess spin and orbital magnetic moments of about 0.46 and $0.34 \mu_B$ per atom, respectively, whereas spin and orbital magnetic moments on other atoms are negligible. By comparing the total energies between FM, AFM and NM states, the FM state is found to be more stable than antiferromagnetic and non-magnetic states. The monolayer ScLiBr_5 has the similar band structure in the presence of SOC as shown in Fig. 3(a). In this case, the monolayer ScLiBr_5 possesses a ferromagnetic ground state with out-of-plane magnetization, and the Curie temperature was estimated to be 67 K by the Monte Carlo simulation based on Eq. (2) with $J_1 = -1.990 \text{ meV}$ and $J_2 = -0.455 \text{ meV}$. The band gap of about 60.2 meV is opened by SOC for monolayer ScLiBr_5 , and it turns into a topologically trivial ferromagnetic semiconductor state with a zero Chern number. By fitting the two bands near Fermi level, we can obtain the parameters for ScLiBr_5 : $\beta/a_1 = -2.3$ and $(\gamma + \eta)/a_3 = -4.6$, which locates in the region of ferromagnetic semiconductor as marked by a dot in Fig. 1(c).

QAHE in LiScX_5 ($X = \text{Cl}, \text{Br}$)—The monolayer LiScX_5 ($X = \text{Cl}, \text{Br}$) can be obtained by exchanging the positions of Li and Sc atoms in the structures of ScLiCl_5 and ScLiBr_5 [Fig. 2(a)]. We shall take LiScCl_5 as a prototypical example because LiScBr_5 shares very similar features. The optimized lattice constant of LiScCl_5 monolayer is $a_0 = 8.0048 \text{ \AA}$. The stability of monolayer LiScCl_5 is also checked by its phonon spectra, molecular dynamics and formation energy (see SM), indicating it is feasible in experiment. By a spin-polarized calculation, we found that the spin magnetic moment carried by LiScCl_5 is about

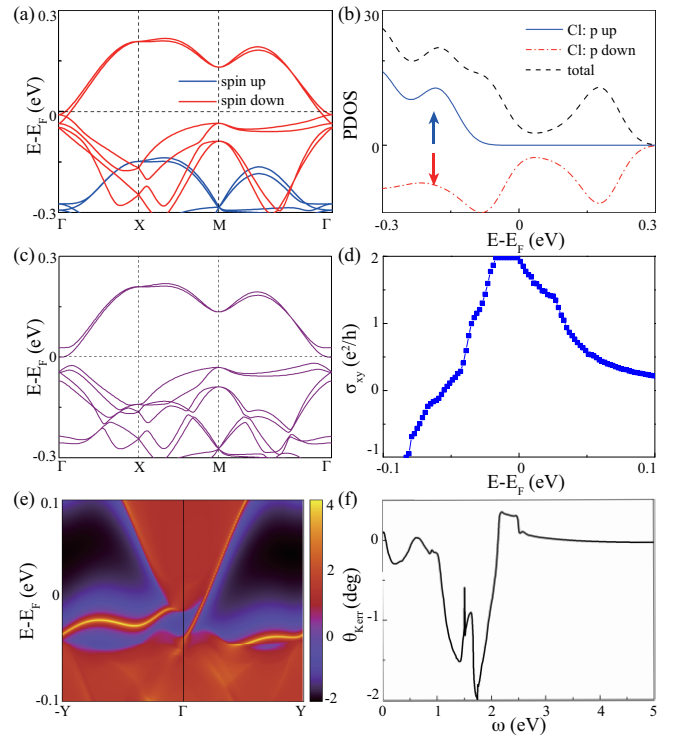


FIG. 4. QAHE in LiScCl_5 monolayer. (a) Band structure in the absence of SOC and (b) partial density of states. (c) The band structure, (d) anomalous Hall conductivity and (e) projected spectrum on (100) surface (line for 2D) with SOC. (f) The Kerr angle θ_{Kerr} as a function of photon energy ω .

$1.54 \mu_B$ per cell shared by all Cl atoms, while the Cl atoms on Wyckoff position $2c$ have orbital moment ($0.03 \mu_B$) much larger than that ($0.01 \mu_B$) for the Cl atoms on Wyckoff position $8g$. Our calculated results show that the FM state is more stable than antiferromagnetic and non-magnetic states.

The electronic band structure and density of states (DOS) for monolayer LiScCl_5 in the absence of SOC are shown in Figs. 4(a) and (b), respectively. It can be seen that the monolayer LiScCl_5 holds the similar band structure as ScLiCl_5 in the presence of SOC except that the band crossing points are closer to the Γ point. From the projected density of states (PDOS) as displayed in Fig. 4(b), we may observe that the states around the Fermi energy are fully polarized in the spin down channel, while the spin up channel has a large gap. The low-energy states are dominated by the p orbitals of all Cl atoms.

In the presence of SOC, the magnetic anisotropy should be considered. By comparing the energies of different magnetization directions, we uncover that the out-of-plane direction is energetically preferred over the in-plane directions, and the energy of out-of-plane magnetization is 1.10 meV lower than that of in-plane magnetization. The Curie temperature is estimated to be 28 K . After tuning on SOC, a gap of about 24.7 meV is

opened as shown in Fig. 4(c). The topologically nontrivial band structure of LiScCl₅ monolayer is characterized by a nonzero Chern number $C = 2$ with a quantized charge Hall plateau $2e^2/h$ and two gapless chiral edge states connecting the valence and conduction bands as shown in Figs. 4(d) and (e), respectively. In addition to the QAHE with high Chern number, the magneto-optical Kerr effect, being a kind of non-contact (non-damaging) optical technique, is a powerful tool for measuring the magnetism in 2D materials^{11,34}. It can be seen that a large Kerr angle θ_{Kerr} is obtained for LiScCl₅ monolayer, particularly for photon energies ω near 1.7 eV as shown in Fig. 4(f). The maximal Kerr angle for LiScCl₅ monolayer is an order of magnitude larger than that for CrGeTe₃ monolayer³⁴, and about 3 times larger than that for bulk Fe³⁵. By fitting the two bands near Fermi level, we can obtain the parameters for LiScCl₅: $\beta/a_1 = -2.0$ and $(\gamma + \eta)/a_3 = -1.9$, which locates in the region of the QAHE as marked by a triangle in Fig. 1(c). The high-Chern-number QAHE with a large band gap of about 113 meV can be also implemented in monolayer LiScBr₅ (see SM).

TABLE I. The differences of matrix element squared between two directions of the magnetization ($|\langle o^- | L_z | u^- \rangle|^2 - |\langle o^- | L_x | u^- \rangle|^2$) and ($|\langle o^+ | L_z | u^- \rangle|^2 - |\langle o^+ | L_x | u^- \rangle|^2$) in Eq. (3), where o and u are occupied and unoccupied orbitals, + and - are majority and minority spin states, respectively.

	$p_{x,+}$	$p_{y,+}$	$p_{z,+}$	$p_{x,-}$	$p_{y,-}$	$p_{z,-}$
$p_{x,+}$	0	1	0	0	-1	0
$p_{y,+}$	1	0	-1	-1	0	1
$p_{z,+}$	0	-1	0	0	1	0
$p_{x,-}$	0	-1	0	0	1	0
$p_{y,-}$	-1	0	1	1	0	-1
$p_{z,-}$	0	1	0	0	-1	0

Magnetic single-ion anisotropy—We shall take ScLiCl₅ as an example to discuss the microscopic mechanism of the out-of-plane magnetization and large magnetic anisotropy.

TABLE II. Orbital-resolved magnetic single-ion anisotropic energy E_{SIA} of Cl atoms in the fully spin-polarized nodal loop semimetal ScLiCl₅, where the dominated E_{SIA} comes from (p_x, p_y) [or (p_y, p_x)] matrix element of Cl atoms on Wyckoff position $2c$.

		(p_x, p_y)	(p_x, p_z)	(p_y, p_z)
Cl	$2c$	3.08	0.10	-0.44
	$8g$	-0.05	0.00	-0.01

According to the second order perturbation theory, the magnetic anisotropy from single-ion anisotropy (SIA) can be described as^{36,37}

$$E_{\text{SIA}} = \lambda^2 \sum_{o,u} \frac{|\langle \psi_u | L_z | \psi_o \rangle|^2 - |\langle \psi_u | L_x | \psi_o \rangle|^2}{\epsilon_u - \epsilon_o}, \quad (3)$$

where λ is the SOC constant, $L_{z/x}$ represent the angular momentum operators, and ϵ_u and ϵ_o are the unoccu-

ped and occupied energy, respectively. A positive value of E_{SIA} indicates the out-of-plane magnetization, otherwise the in-plane. Equation (3) means that the orbitals near the Fermi energy mainly contribute to MAE. By calculating the differences of matrix element squared between two directions of the magnetization for p orbitals according to Eq. (3) as shown in Table I, we note that the contributions to MAE from the same spins and from the opposite spins between occupied ($|\psi_o\rangle$) and unoccupied ($|\psi_u\rangle$) states have opposite signs. Positive and negative matrix elements prefer the out-of-plane and in-plane magnetization, respectively. In our systems, the states near the Fermi energy are mainly contributed by the same spin (spin down) of $p_{x,y}$ orbitals, which should prefer an out-of-plane magnetization.

To confirm the above observation, the orbital-resolved E_{SIA} was calculated for ScLiCl₅ monolayer as listed in Table II. It is seen that Li and Sc atoms as well as Cl atoms on Wyckoff position $8g$ make no contribution to E_{SIA} , while the main contribution comes from Cl atoms on Wyckoff position $2c$ as revealed in Table II. The value of (p_x, p_y) matrix element is dominated and positive, indicating an out-of-plane magnetization, which is consistent with the above analysis. For monolayers ScLiBr₅ and LiScX₅ (X=Cl, Br), the same analysis applies and we find that they all prefer the out-of-plane magnetization, which is consistent with our DFT results.

Conclusion—In this work, we propose the p -orbital topological magnetic states on a square lattice with space group $P/4n$ by means of the symmetries and $k \cdot p$ model analyses that are materials-independent. Three currently interested topological states, including topological semimetal, QAHE and topologically trivial ferromagnetic semiconductor, can be obtained on the square lattice, depending on the interplay between different SOC parameters. A phase diagram is presented. As examples, we show that the above three different topological states can be indeed implemented in 2D materials ScLiCl₅, ScLiBr₅ and LiScCl₅ (or LiScBr₅), respectively. Furthermore, the ferromagnetism of these 2D ferromagnets is unveiled from the p -orbitals of halogen elements, and the microscopic origin of ferromagnetism from p electrons is elaborated. This present study opens a door to explore not only exotic topological states (e.g. nodal loop half-semimetal) but also the quantum magnetism from p -orbital electrons in terms of the model and materials-independent analyses.

Acknowledgements—This work is supported in part by the National Key R&D Program of China (Grant No. 2018YFA0305800), the Strategic Priority Research Program of the Chinese Academy of Sciences (Grant No. XDB28000000), the National Natural Science Foundation of China (Grant No.11834014), and Beijing Municipal Science and Technology Commission (Grant No. Z191100007219013). B.G. is also supported by the National Natural Science Foundation of China (Grants No. Y81Z01A1A9 and No. 12074378), the Chinese Academy of Sciences (Grants No. Y929013EA2 and No.

E0EG4301X2), the University of Chinese Academy of Sciences (Grant No. 110200M208), the Strategic Pri-

ority Research Program of Chinese Academy of Sciences (Grant No. XDB33000000), and the Beijing Natural Science Foundation (Grant No. Z190011).

- ¹ F. D. M. Haldane, *Phys. Rev. Lett.* **61**, 2015 (1988).
- ² M. Onoda and N. Nagaosa, *Phys. Rev. Lett.* **90**, 206601 (2003).
- ³ C.-X. Liu, X.-L. Qi, X. Dai, Z. Fang, and S.-C. Zhang, *Phys. Rev. Lett.* **101**, 146802 (2008).
- ⁴ K. He, Y. Wang, and Q.-K. Xue, *Annu. Rev. Condens. Matter Phys.* **9**, 329 (2018).
- ⁵ C.-X. Liu, S.-C. Zhang, and X.-L. Qi, *Annu. Rev. Condens. Matter Phys.* **7**, 301 (2016).
- ⁶ X. Kou, Y. Fan, M. Lang, P. Upadhyaya, and K. L. Wang, *Solid State Commun.* **215-216**, 34 (2015).
- ⁷ J. Wu, J. Liu, and X.-J. Liu, *Phys. Rev. Lett.* **113**, 136403 (2014).
- ⁸ C. Wu, *Phys. Rev. Lett.* **101**, 186807 (2008).
- ⁹ R. Yu, W. Zhang, H.-J. Zhang, S.-C. Zhang, X. Dai, and Z. Fang, *Science* **329**, 61 (2010).
- ¹⁰ C.-Z. Chang, J. Zhang, X. Feng, J. Shen, Z. Zhang, M. Guo, K. Li, Y. Ou, P. Wei, L.-L. Wang, Z.-Q. Ji, Y. Feng, S. Ji, X. Chen, J. Jia, X. Dai, Z. Fang, S.-C. Zhang, K. He, Y. Wang, L. Lu, X.-C. Ma, and Q.-K. Xue, *Science* **340**, 167 (2013).
- ¹¹ C.-Z. Chang, J. Zhang, M. Liu, Z. Zhang, X. Feng, K. Li, L.-L. Wang, X. Chen, X. Dai, Z. Fang, X.-L. Qi, S.-C. Zhang, Y. Wang, K. He, X.-C. Ma, and Q.-K. Xue, *Adv. Mater.* **25**, 1065 (2013).
- ¹² L. Si, O. Janson, G. Li, Z. Zhong, Z. Liao, G. Koster, and K. Held, *Phys. Rev. Lett.* **119**, 026402 (2017).
- ¹³ J. He, S. Ma, P. Lyu, and P. Nachtigall, *J. Mater. Chem. C* **4**, 2518 (2016).
- ¹⁴ C. Huang, J. Zhou, H. Wu, K. Deng, P. Jena, and E. Kan, *Phys. Rev. B* **95**, 045113 (2017).
- ¹⁵ J. He, X. Li, P. Lyu, and P. Nachtigall, *Nanoscale* **9**, 2246 (2017).
- ¹⁶ Q. Sun and N. Kioussis, *Phys. Rev. B* **97**, 094408 (2018).
- ¹⁷ Y. ping Wang, S. shi Li, C. wen Zhang, S. feng Zhang, W. xiao Ji, P. Li, and P. ji Wang, *J. Mater. Chem. C* **6**, 10284 (2018).
- ¹⁸ J.-Y. You, Z. Zhang, B. Gu, and G. Su, *Phys. Rev. Appl.* **12**, 024063 (2019).
- ¹⁹ Y. Li, J. Li, Y. Li, M. Ye, F. Zheng, Z. Zhang, J. Fu, W. Duan, and Y. Xu, *Phys. Rev. Lett.* **125**, 086401 (2020).
- ²⁰ C.-Z. Chang, W. Zhao, D. Y. Kim, H. Zhang, B. A. Assaf, D. Heiman, S.-C. Zhang, C. Liu, M. H. W. Chan, and J. S. Moodera, *Nat. Mater.* **14**, 473 (2015).
- ²¹ Y. Ou, C. Liu, G. Jiang, Y. Feng, D. Zhao, W. Wu, X.-X. Wang, W. Li, C. Song, L.-L. Wang, W. Wang, W. Wu, Y. Wang, K. He, X.-C. Ma, and Q.-K. Xue, *Adv. Mater.* **30**, 1703062 (2017).
- ²² M. Mogi, R. Yoshimi, A. Tsukazaki, K. Yasuda, Y. Kozuka, K. S. Takahashi, M. Kawasaki, and Y. Tokura, *Appl. Phys. Lett.* **107**, 182401 (2015).
- ²³ J. Li, Y. Li, S. Du, Z. Wang, B.-L. Gu, S.-C. Zhang, K. He, W. Duan, and Y. Xu, *Sci. Adv.* **5**, eaaw5685 (2019).
- ²⁴ Y. Deng, Y. Yu, M. Z. Shi, Z. Guo, Z. Xu, J. Wang, X. H. Chen, and Y. Zhang, *Science* **367**, 895 (2020).
- ²⁵ J. Ge, Y. Liu, J. Li, H. Li, T. Luo, Y. Wu, Y. Xu, and J. Wang, *Natl. Sci. Rev.* **7**, 1280 (2020).
- ²⁶ C. Liu, Y. Wang, H. Li, Y. Wu, Y. Li, J. Li, K. He, Y. Xu, J. Zhang, and Y. Wang, *Nat. Mater.* **19**, 522 (2020).
- ²⁷ P. Kierkegaard, J. M. Longo, C. J. Ballhausen, U. Ragnarsson, S. E. Rasmussen, E. Sunde, and N. A. Sørensen, *Acta Chem. Scand.* **24**, 427 (1970).
- ²⁸ M. Tachez, F. Theobald, and E. Bordes, *J. Solid State Chem.* **40**, 280 (1981).
- ²⁹ L. Lezama, G. Villeneuve, M. Marcos, J. Pizarro, P. Hagenmuller, and T. Rojo, *Solid State Commun.* **70**, 899 (1989).
- ³⁰ T. Amos, A. Yokochi, and A. Sleight, *J. Solid State Chem.* **141**, 303 (1998).
- ³¹ P. Carretta, N. Papinutto, C. B. Azzoni, M. C. Mozzati, E. Pavarini, S. Gonthier, and P. Millet, *Phys. Rev. B* **66**, 094420 (2002).
- ³² P. Carretta, N. Papinutto, C. Azzoni, M. Mozzati, E. Pavarini, S. Gonthier, and P. Miller, *Acta Phys. Pol. B* **34**, 1407 (2003).
- ³³ A. Kiani and E. Pavarini, *Phys. Rev. B* **94**, 075112 (2016).
- ³⁴ C. Gong, L. Li, Z. Li, H. Ji, A. Stern, Y. Xia, T. Cao, W. Bao, C. Wang, Y. Wang, Z. Q. Qiu, R. J. Cava, S. G. Louie, J. Xia, and X. Zhang, *Nature* **546**, 265 (2017).
- ³⁵ G. S. Krinchik and V. A. Artem'Ev, *J. Exp. Theor. Phys.* **26**, 1080 (1968).
- ³⁶ D. sheng Wang, R. Wu, and A. J. Freeman, *Phys. Rev. B* **47**, 14932 (1993).
- ³⁷ B. S. Yang, J. Zhang, L. N. Jiang, W. Z. Chen, P. Tang, X.-G. Zhang, Y. Yan, and X. F. Han, *Phys. Rev. B* **95**, 174424 (2017).